Plasmonic Properties of SrVO₃ Bulk and Nanostructures

Chia-Ping Su, Kari Ruotsalainen, Alessandro Nicolaou, Matteo Gatti, and Alexandre Gloter*

Correlated metals, such as $SrVO_3$ (SVO) or $SrNbO_3$, are promising materials for optical devices such as transparent conductors. Here, a real-space and reciprocal-space electron-energy-loss-spectroscopy (EELS) investigation of SVO bulk and nanostructures is reported. An intense 1.35 eV excitation with a weak energy dispersion is observed in the loss function and is attributed to a bulk plasmonic excitation from the 3d-t_{2g} orbitals. Ab initio calculations done within a time-dependent density functional theory framework reveal that a 1.5 band renormalization is sufficient to reproduce quantitatively this d–d plasmon energy and dispersion. The corresponding localized surface plasmon (LSP) peaks are measured by EELS on various nanostructures and are compared to finite-difference time-domain simulations. These LSPs exhibit quality factors above canonical materials (e.g., indium tin oxide) in the near-infrared regime, demonstrating that SVO is also a material of high interest for plasmonic applications. Finally, by phasing out the surface plasmon contribution with EELS collected at minute off-dipolar conditions, the bulk-type plasmonic values are retrieved with nanometrical resolution. Core–shelled electronic structures are then observed for nanorods designed by focused ion beam (FIB), revealing a bandgap opening due to FIB damage. It is envisioned that similar bulk measurement can be feasible for most of the transition metal oxide nanostructures.

C.-P. Su, A. Gloter
Laboratoire de Physique des Solides
CNRS
Université Paris-Saclay
Orsay 91405, France
E-mail: alexandre.gloter@u-psud.fr
K. Ruotsalainen, A. Nicolaou, M. Gatti
Synchrotron SOLEIL
L'Orme des Merisiers
Saint-Aubin, Boîte Postale 48, Gif-sur-Yvette F-91192, France
M. Gatti
LSI
CNRS
CEA/DRF/IRAMIS
École Polytechnique
Institut Polytechnique de Paris
Palaiseau F-91120, France
M. Gatti
European Theoretical Spectroscopy Facility (ETSF)

1. Introduction

Correlated metals, such as $SrVO_3$ (SVO) or $SrNbO_3$, are promising materials for transparent conductors.[1,2] SVO has good conductivity, in the range of ≈10^{-4} Ω cm with ≈2×10^{22} cm^{-3} carrier densities at room temperature.[3] SVO thin films can be further modulated by growth conditions,[4] strain, or film thickness, down to a reported metal–insulator transition (MIT) for ultrathin SVO films under tensile strain.[5] In correspondence to this transport property, remarkable optical transparency has been reported in the visible range indicating SVO as a possible new transparent conductive oxide.[1–3] The transparency is effective since the absorption due to transitions from the O-2p to the V-3d empty bands (p–d excitations a.k.a. charge transfer excitations) is located above the visible range while the plasmons and the transitions associated with the electrons within the V-t_{2g} bands (d–d excitations) remain located in the infrared (IR) range. In the seminal work of Makino et al.[6] on the optical properties of the $Ca_{1-x}Sr_xVO_3$ solid solution, a plasmon peak of 1.3 eV was inferred for SVO. It was described within a Drude model for a 1.7×10^{22} cm^{-3} charge density (corresponding to a V-d^1 occupation within a perovskite unit cell volume) and a renormalized effective mass m^* of ≈3, due to electronic correlation. Such a concept is at the base of the view of correlated metals as new transparent conductors, when compared to doped oxide semiconductors such as tin-doped indium oxide (ITO). While the latter has low electron densities, correlated metals have a large amount of charge but plasmon energy below the optical range due to enhanced effective mass by correlation effects.[1] Electronic correlations are associated with the bandwidth narrowing in transition metal oxides (TMO) and since the bandwidth can be controlled, for example, by a structural parameter, the optical properties of these correlated metals have been tentatively tuned by strain. In 2019, Mirjolet et al.[7] and Boileau et al.[8] reported a plasmon redshift and then increased visible transparency for SVO grown on a $SrTiO_3$ substrate. It is associated with a significant mass enhancement up to $m^* = 5$. This modulation is due to symmetry selection within the t_{2g} orbitals and to band narrowing due to tensile strain from the $SrTiO_3$ substrate.[7] In the case of the vanadium Wadsley conductors (VO_2(B) and V_6O_{13}), Choi et al.[9] also proposed an enhancement of the IR–visible transparency attributed to a

redshift of the plasma frequency induced by the correlated electrons. On the other hand, the higher transparency of SrNbO$_3$ (4d^1) in the UV side is attributed to a lower shift of the plasmon due to a smaller mass renormalization for the Nb-4d^1 configuration as compared to the V-3d^1 configuration of SVO.[2] While electron correlations clearly play a role in the plasmon energy of 3d or 4d TMO, many questions remain open. In particular, the amount of the mass renormalization is often parametrized within an extended Drude model by comparing the plasmon energy extracted from optical conductivity measurements with the plasmon energy or the effective mass obtained from density functional theory (DFT) ground state calculations.[1,2]

The occurrence of a strong bulk plasmonic excitation at low energy is also of interest for the interpretation of signatures of dynamical correlation in the photoemission spectra of SVO. Indeed, SVO is considered as the prototype of a strongly correlated metal, and photoemission spectroscopy (PES)[10,11] and inverse-photoemission spectroscopy (IPES)[12] have shown satellites located outside the renormalized quasiparticle band. An abundance of works has interpreted these satellites as Hubbard bands, notably as they appear as the incoherent parts of the calculated dynamical mean-field theory (DMFT) spectral function.[13–15] Conversely, several recent works have suggested that these satellite peaks originate from the coupling of the quasiparticles with neutral collective low-energy d–d excitations.[16–18] Based on many-body perturbation theory, Gatti and Guzzo[16] demonstrated that the photo-emission satellite located at ≈1.5 eV below the Fermi level is associated with a peak in the loss function, presumably a d–d plasmon at similar energy. In this article, we will report the energy and dispersion of the bulk d–d plasmon in SVO as measured by electron energy loss spectroscopy.

Furthermore, in the case of metallic nanostructures, surface plasmons also occur. They have not yet been reported for SVO nanostructures, while other transparent conductive oxides, such as aluminum-doped zinc oxide (AZO), gallium-doped zinc oxide (GZO), or ITO, are already investigated as possible substitutes to noble metals for low-loss plasmonic and metamaterial applications in the near-IR regime.[19] Nanostructuration of the transparent electrodes (e.g., AZO)[20] is also a strategy to increase its visible transmittance. A figure of merit for the engineering of this localized surface plasmon (LSP) resonance is its quality factor (Q-factor), defined as the ratio of LSP peak energy to its line width. Monochromated scanning transmission electron microscopy (STEM) and electron energy loss spectroscopy (EELS), which are combining high spatial resolution (sub-nanometric) and high energy resolution (≈10 meV), have recently been used to measure the Q-factors of LSP, mostly for traditional plasmonic metals such as Au,[21] Ag, or Cu.[22] The Q-factors can be measured at the scale of individual objects or even for each resonance. At low energy, the LSP can extend several tens of nanometers away from the metal surface due to the delocalization of the excitations. We will measure by STEM–EELS the Q-factors and the spatial distribution of the LSP of SVO nanostructures.

While the investigation of these surface plasmons is of interest for optical applications, the quantitative measurement of bulk d–d plasmon excitations with the nanometer-scale resolution is of interest from a solid-state physics point of view,

where, for example, an MIT can occur at nanodomain or interface.[23] In principle, bulk plasmons are expected to be more spatially localized, notably when probed through non-dipolar transitions. Nevertheless, while dipolar excitations can be easily measured due to a large cross-section, non-dipolar measurements are more difficult to access due to experimental and theoretical constraints (lower cross-section, strong dynamical electron diffraction, requirement of simultaneous nanometric and angular resolution, energetic dispersion with the scattering angle, etc.). Correlated metals have a low band dispersion and the corresponding bulk plasmon is expected to have a small energetic dispersion as well. We will use these properties to obtain a nanometrical measurement of bulk-type excitations in SVO by minute off-dipolar EELS collection. We expect that such an approach can extend to most TMO cases.
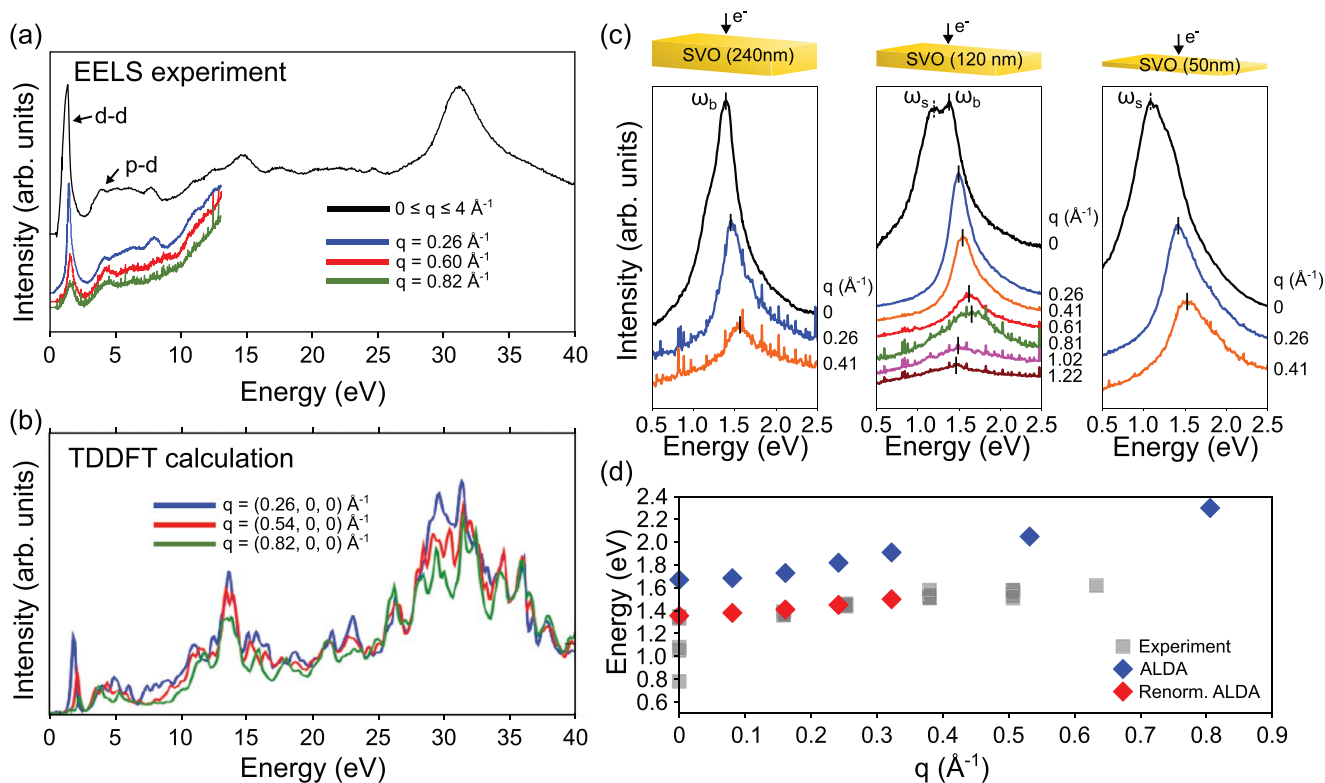
To summarize, in this article, we address the three following issues: i) Is the 1.35 eV loss excitation of SVO a bulk plasmon with a small energy dispersion and how important are electronic correlations that have to be included for reaching plasmon energy below the optical regime? ii) What are the quality factors of SVO LSPs and how do they compare with other alternative plasmonic materials? iii) How can EELS be efficient to measure the "bulk" type plasmon energy on TMO nanostructure with nanometric resolution?

To answer these questions, we have done STEM–EELS measurements on bulk and nanostructured SVO. The EELS have been done with spatial, angular, or combined resolution. The experiments are then discussed with the help of ab initio calculations of the dielectric function obtained within the adiabatic local-density approximation (ALDA) of time-dependent density-functional theory (TDDFT).[24] Surface plasmon EELS resonances are then simulated using the finite-difference time-domain method (FDTD)[25,26] and compared to EELS experimental maps.

2. Results and Discussions

Figure 1a shows the EELS spectrum (black curve) measured for micrometrical particles of SVO at a distance of more than 300 nm from any lateral surfaces, and with a local thickness above 300 nm. The spectrum has been corrected from the multiple plasmons scattering expected for such thickness and shows several well-identified features spanning from ≈1 to 40 eV, among them, a very narrow and intense peak at ≈1.35 eV. The EELS spectra (1–15 eV) collected at different scattering angles are also visible in Figure 1a and are in overall good agreement with the TDDFT calculation of the loss function (Figure 1b). The peaks at ≈1.35 eV (experiment) and ≈1.7 eV (theory) are associated with a plasmonic peak within the t$_{2g}$ bands (noted as d–d) and the structures at ≈3 eV (experiment and theory) correspond to transitions from the O-2p band to the V-d empty states (noted p–d), the dip in-between them being the EELS analog of the visible transparency.

Plasmon peaks were measured for slabs with different but homogeneous thicknesses (thickness t of ≈240, 120, and 50 nm) as obtained by focused ion beam (FIB) polishing. First, at q equal to zero, the thicker slab (Figure 1c, t = 240 nm) shows a bulk plasmon peak at 1.35 eV and an energy dispersion

ADVANCED
SCIENCE NEWS
www.advancedsciencenews.com

ADVANCED
OPTICAL
MATERIALS
www.advopticalmat.de

Figure 1. a) Experimental EELS loss function measured on micro-crystal. b) Simulated loss function obtained by time-dependent density-functional theory (TDDFT) using the adiabatic local-density approximation (ALDA). c) Experimental EELS loss function of the d–d plasmon excitations for FIB-derived slabs of different thicknesses. d) Comparison of the energy dispersion of the experimental d–d plasmons with the ALDA and renormalized ALDA simulations. For the calculations, the values at $q = 0$ have been estimated by interpolating the values with a fit following a q^2 dispersion. When thickness effects are made negligible in the experimental EELS (i.e., for thick slabs or non-dipolar condition), a renormalization of the t_{2g} bands of 1.5 gives a quantitative match with the experiments. Throughout this work, the reciprocal lattice vector is expressed as $2\pi/a$ (Å^{-1}), where a is the lattice parameter. The momentum transfers are defined accordingly.

in agreement with the results obtained for large particles (Figure 1a), confirming the bulk nature of these measurements. The slab with a thickness of 120 nm already exhibits a very strong additional plasmonic feature at ≈1.1 eV that corresponds to the surface plasmons probed by the electron beam at the entrance and exit planes of the slabs. For the transferred scattering vector of $q = 0.26$ Å^{-1}, the intensity of this surface plasmon is vanishing and spectral features similar to the bulk type are retrieved. The thinner slab of ≈50 nm exhibits only a surface plasmon of ≈0.9 eV when probed with dipolar transition, while a plasmon in the range of ≈1.4 eV is retrieved for non-dipolar conditions. The rapid disappearance of the surface plasmon at $q > 0$ is rather consistent with the intensity decrease of surface plasmons with q^{-3}.[27,28] For dipolar conditions, the transfer of spectral intensity from the bulk plasmon to the surface plasmon (e.g., for the SVO slab with $t = 50$ nm) and the thickness dispersion of the plasmon energies have been reported for other thin films.[28,29] However, it is here to note that the effect is stronger than reported for noble metals. For instance, Gong et al.[29] reported that the thickness dispersion becomes negligible for silver thin films above 20 nm while it is still prevailing in the case of SVO at similar thickness.

Figure 1d comprises the dispersion curves from different slabs. At $q = 0$, the surface plasmon energies span from 0.7 to 1.2 eV (due to the thickness dispersion), with a bulk plasmon observed at ≈1.35 eV. On the other hand, the energy differences for all the slabs become lower than 40 meV for transferred momentum in the 0.15 to 0.70 Å^{-1} regimes accessible in our EELS experiment. These dispersion curves evidence that the d–d plasmon has a small energy dispersion of ≈170 meV across 0.5 Å^{-1}. This is much lower than the plasmon energy dispersion measured for In (≈0.6 eV over 0.5 Å^{-1}), Al (≈0.35 eV over 0.5 Å^{-1}),[30] Ag (≈0.3 eV over 0.4 Å^{-1}),[31] or black phosphorus (≈1 eV over 0.1 Å^{-1})[32] and is not surprising for a correlated metal with V-d bands of limited dispersions. Negative plasmon dispersions have even been reported for Cs in relation to its low electron density,[33] and for layered transition-metal dichalcogenides (2H-TaSe$_2$, ≈−100 meV over 0.5 Å^{-1}) where narrow d bands are also present.[34] Resonant inelastic X-ray scattering of vanadates, such as CaVO$_3$ or LaVO$_3$, has reported excitations at ≈2 eV, corresponding to crystal-field excitations within a 3d^1 or 3d^2 configuration.[35,36] Nevertheless, the dispersion of the SVO EELS excitation is larger than the one reported for d–d crystal-field excitations that can be interpreted as a nearly atomic transition within multiplet terms. For instance, an energy dispersion below 100 meV over 7 Å^{-1} has been reported by non-resonant inelastic X-ray scattering for the d–d excitations in CoO and NiO.[37] It also confirms that the d–d excitations observed

ADVANCED
SCIENCE NEWS
www.advancedsciencenews.com

ADVANCED
OPTICAL
MATERIALS
www.advopticalmat.de

in SVO are more of a plasmonic character than intra-atomic transitions within V-d^1 multiplet terms. The plasmonic character is also evidenced in the dielectric function ($\varepsilon = \varepsilon' + i\varepsilon''$) as obtained in the TDDFT calculation where its real part crosses zero at an energy close to the observed loss peak (Figure S1, Supporting Information). Nevertheless, when comparing the absolute experimental energy and dispersion from the calculations obtained in TDDFT, a blueshift of 300 meV and a stronger dispersion is obtained in the simulation (ALDA curve in Figure 1d). These overestimations by the theory are due to the following two approximations in the ab initio simulation: i) the LDA for the ground-state DFT calculation; ii) the ALDA for the linear-response TDDFT calculation of the spectrum. Both are known to yield a blueshift of plasmon energies in metals.[38] In order to apply a simple correction, the spectra have been simulated within the ALDA with a bandwidth reduced by a factor of 1.5 (Figure 1d, renorm. ALDA). The main effect is the redshift of the plasmon peaks (the result of a simple parabolic fit of the positions of maxima of the peaks as a function of q estimates the plasmon energy at $q = 0$ at 1.35 eV, while in the original ALDA it is 1.67 eV). The plasmon dispersion is also reduced from 0.3 to 0.13 eV over 0.32 Å^{-1}. Those values are in excellent agreement with the experimental data and have been obtained with a band renormalization that is smaller than the value of 2 suggested by DMFT calculations of the quasiparticle band.[2,39,40]

Strong surface plasmons were already present for quasi-infinite slabs in Figure 1c and we will investigate for different nanostructures how SrVO$_3$ can sustain LSPs. **Figure 2**a,b reports the evolution of the EELS low-loss spectra when

crossing the surface of a thick microparticle ($t > 200$ nm). While the loss at ≈100 nm from the surface has almost no surface contribution, an intense surface plasmon is visible when the electron is traveling at the surface or outside the particle (in an aloof geometry). When probed from the vacuum, the bulk excitations below 10 eV have redshifted to the corresponding surface excitations, whose intensities decay with the energy. Figure 2c,d reports the case at the edge surface of a slab ($t < 100$ nm as obtained by FIB). In addition to the surface state (B), edge states (A$_1$, A$_2$) are visible and survive at rather far distances from the surfaces. The FDTD simulation (Figure 2e,f) captures the trends, but a single edge state only is visible in the energy range of the calculation due to the approximation in the slab shape. Nevertheless, the presence of several plasmons at different energies is similar to the case of a classical noble metal, such as Ag, where edges and surface states were observed for flat nanostructure.[41] The EELS measurements and calculations of Figure S2, Supporting Information, for different flat nanostructures clearly indicate that most energy modes are accessible in the 0.4 to 1.2 eV range depending on the slab geometry and edge lengths. In order to compare the SVO surface plasmon quality with existing materials and notably the other transparent conducting oxides, EELS measurements have been done on more regular rod-like nanostructures, whose plasmon modes are expected closer to Fabry–Pérot types. Two kinds of nanostructures were obtained by FIB: half-rods (rods that connect with a vast substrate) and nanoslits, which are complementary systems of the nanorods notably via a Babinet reciprocity principle[42] (see images of typical nanostructures in Figure S3, Supporting Information).
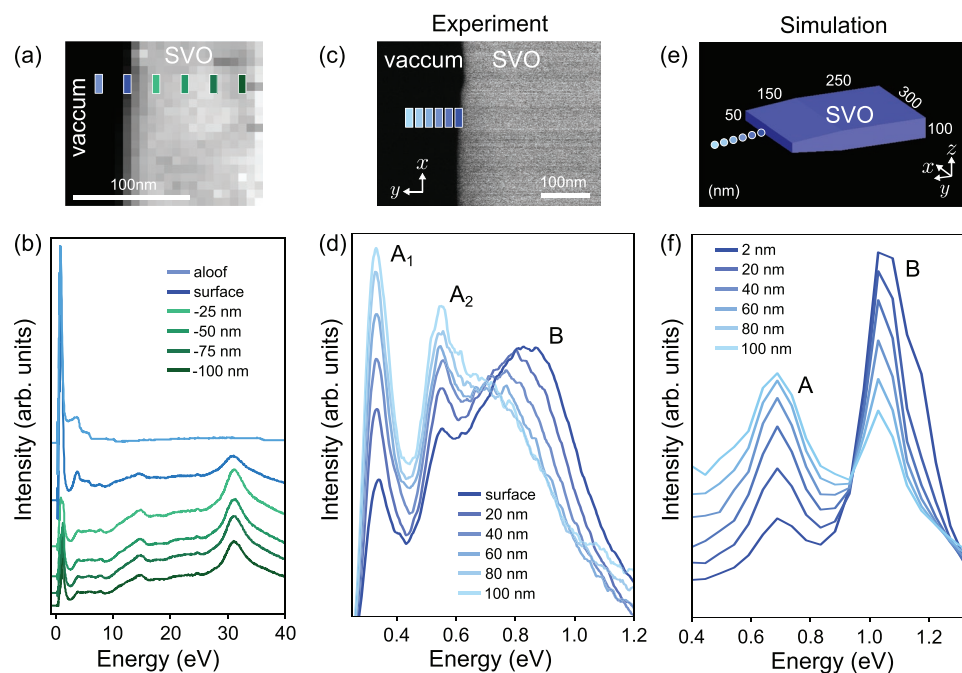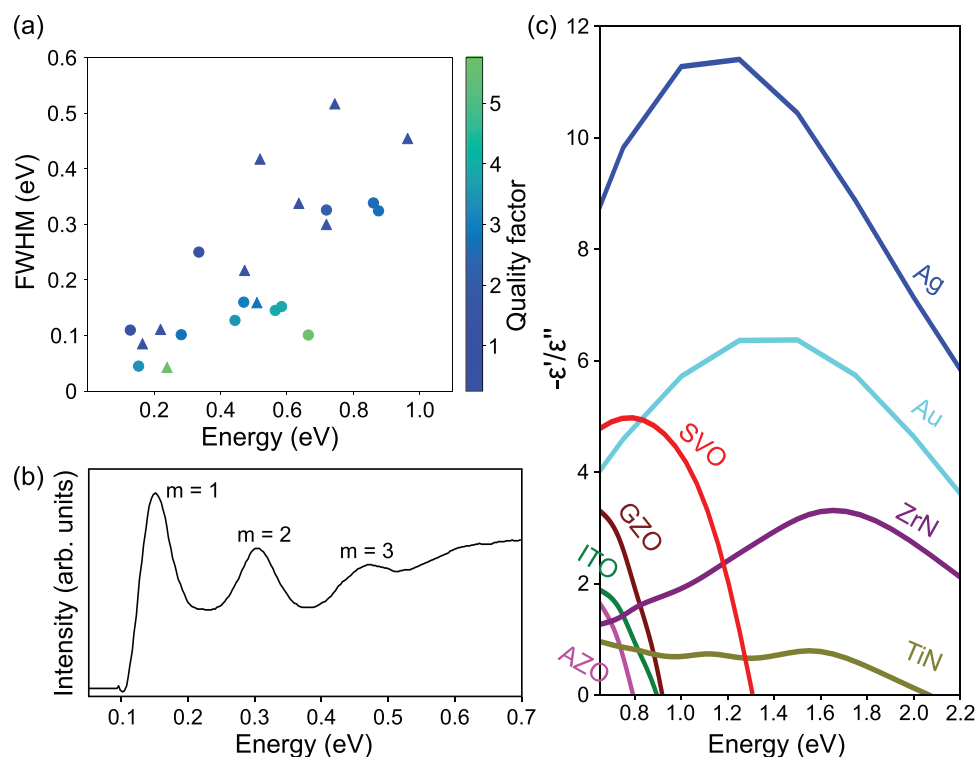

Figure 2. a,b) STEM-high-angle annular dark-field (HAADF) images of the surface of an SVO microcrystal (local thickness > 200 nm). Series of EELS spectra (0–40 eV), when the probe is raster from the inner part (−100 nm from the surface) to the vacuum (aloof geometry). c,d) STEM-HAADF and corresponding EELS spectra (d–d plasmon) obtained near the edge of a slab of thickness <100 nm. Each spectrum is taken from the position with corresponding colors marked in (c). e,f) FDTD simulation of the EELS loss near an edge with the model geometry shown at the top. For both experimental and simulation, the spatial dependence of the spectra is obtained with impact parameters from 2 (dark blue) to 100 nm (light blue).
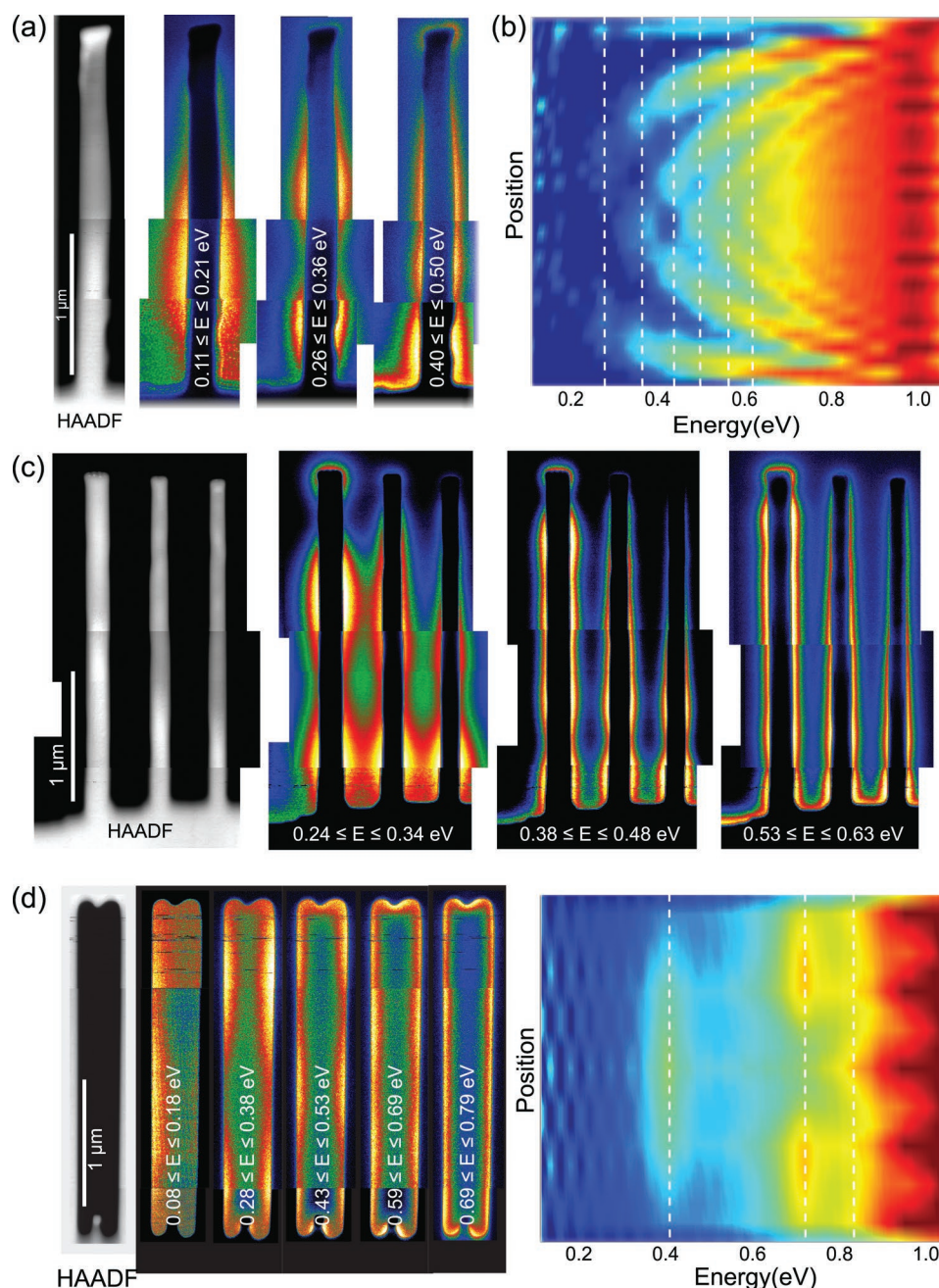
Figure 3. a) HAADF-STEM image and experimental EELS energy filtered map of a 2.5 µm length half-rod. b) Simulated EELS spectra along a half-rod of 2.5 µm with an aspect ratio of ≈25. c) HAADF-STEM image and experimental EELS energy-filtered images of 2.5 µm length triple half-rods. d) HAADF-STEM image and experimental EELS energy-filtered images of a 2.5 µm length slit along with a simulated EELS map. All scale bars are 1 µm.

Figure 3a shows the experimental EELS maps obtained for an isolated half-rod of ≈2500 nm long, where several LSP modes are observed. A mode with an energy of ≈160 meV has a single intensity maximum displaced to the lower part of the half-rod, while more nodes appear for higher energy plasmons. The asymmetric distribution (i.e., the lower mode is not at the center of the half-rod) is also observed in the calculation of Figure 3b. This asymmetric spatial distribution is modulated by the aspect ratio of the half-rod (see Figure S4, Supporting Information) and the small discrepancy between calculation and

experiment (Figure 3a,b) is certainly due to a mismatch in the geometric model. Indeed, as discussed later, the FIB-designed nanostructures are suffering from a large surface layer where the bulk SVO electronic and optical structures are not maintained. This layer was not included in the FDTD simulation. Figure 3c reveals the surface plasmon spatial distributions for three neighboring half-rods. Every rod has slightly different widths and the modes maxima are spatially gliding (notably for the mode at ≈300 meV) confirming that small changes in the aspect ratio can change rather efficiently the position and

ADVANCED
SCIENCE NEWS

www.advancedsciencenews.com

ADVANCED
OPTICAL
MATERIALS

www.advopticalmat.de

Figure 4. a) Full-width at half-maximum (FWHM) and the corresponding quality factors of surface plasmon resonances for half-rods (symbol of the triangle) and slits (symbol of the circle) of different sizes. FWHM is estimated by fitted with a Lorentzian function. b) Typical EELS spectrum of a slit showing clearly three modes whose FWHM are below 100 meV. c) Energy dependence of $-\varepsilon'/\varepsilon''$ for several plasmonic materials.

energy of these plasmons (see also Figure S4, Supporting Information). The case of EELS measurement for a slit is in Figure 3d. As expected from the Babinet principle, the lowest energy mode is not at the tip of the slit but appears at the center of the slit. At the upper and lower part of the slit are present small protuberances, showing local enhancement of the electromagnetic field typical of plasmonic hot spots. These different positions of the nodes within the slit are confirmed by the calculations (see for instance the comparison of the plasmon distribution between the slits versus the rods as calculated for different aspect ratios in Figure S4, Supporting Information).

In order to evaluate the quality of the surface plasmon resonances on these structures, the quality factors of each plasmon mode have been calculated for these samples, by estimating $Q \approx \omega_p/\Gamma$ where ω_p is the energy of the surface plasmon resonance mode, and Γ its FWHM. The quality factor is in the range of $Q = 3–5$ for energies around 0.4 to 0.7 eV (**Figure 4**a) and many modes are exhibiting FWHM lower than 100 meV (Figure 4b). These estimations of quality factors can be seen as rather conservative since the energy broadening of the EELS source ($\Delta E = 40$ meV) has not been deconvoluted and the nanostructures engineered by FIB have damaged surfaces and inhomogeneous shape (e.g., half-rod have some conic shape). Nevertheless, these values are very close to best-reported cases for noble metals or metallic oxides, even for nanostructures obtained by chemical route or optimized for their optical properties, indicating the potential of SVO for plasmonic engineering. Quality factors of about 5 at 0.5 eV of plasmon energies had been reported by EELS for gold rods[21] and more recently a

Q of about 4 was reported for silver rods with lower plasmon energies (0.3 eV).[22] For comparison with metallic oxides, STEM–EELS measurements in lithographed nanostructures of ITO triangle reveal LSP excitations between 150 and 550 meV (for a ≈730 meV bulk plasmon) with damping Γ in the range of 150 meV.[43] Runnerstrom et al.[44] compared Q-factors of Ce- and Sn-doped indium oxide nanocrystals obtained by chemistry. They reported that the LSP peaks are exceptionally narrow and symmetric with Ce doping, with the narrowest peak occurring for nanocrystals doped with 5.2% Ce, which display an LSP peak at 310 meV with a width of only 77 meV (giving a quality factor of ≈4). Similar Q-factors have also been recently reported from EELS measurement of $(Ba,La)SnO_3$ nanorods.[45] Highly doped $(Ba,La)SnO_3$ support plasmons up to 0.8 eV associated with electrons being injected in the conduction band consisting primarily of Sn 5s state. The case of $SrVO_3$ is very different from these doped semiconductors.

As mentioned earlier, the plasmon in SVO originates from the V 3d^1 configuration with a very different electronic structure as compared to the doped semiconducting oxides. The quality factor of the LSP depends on many parameters,[21] notably the geometry of the object.[22] For spherical nanoparticles, it has been reported that part of the quality factor can be discussed by comparing the evolution of $-\varepsilon'/\varepsilon''$[46] and the case of SVO is compared with some other plasmonic materials in Figure 4c. The very specific position of the SVO with respect to the doped semiconducting oxides, metal nitrides, or noble metals is evident and emphasizes the high potential of SVO as an IR plasmonic material.
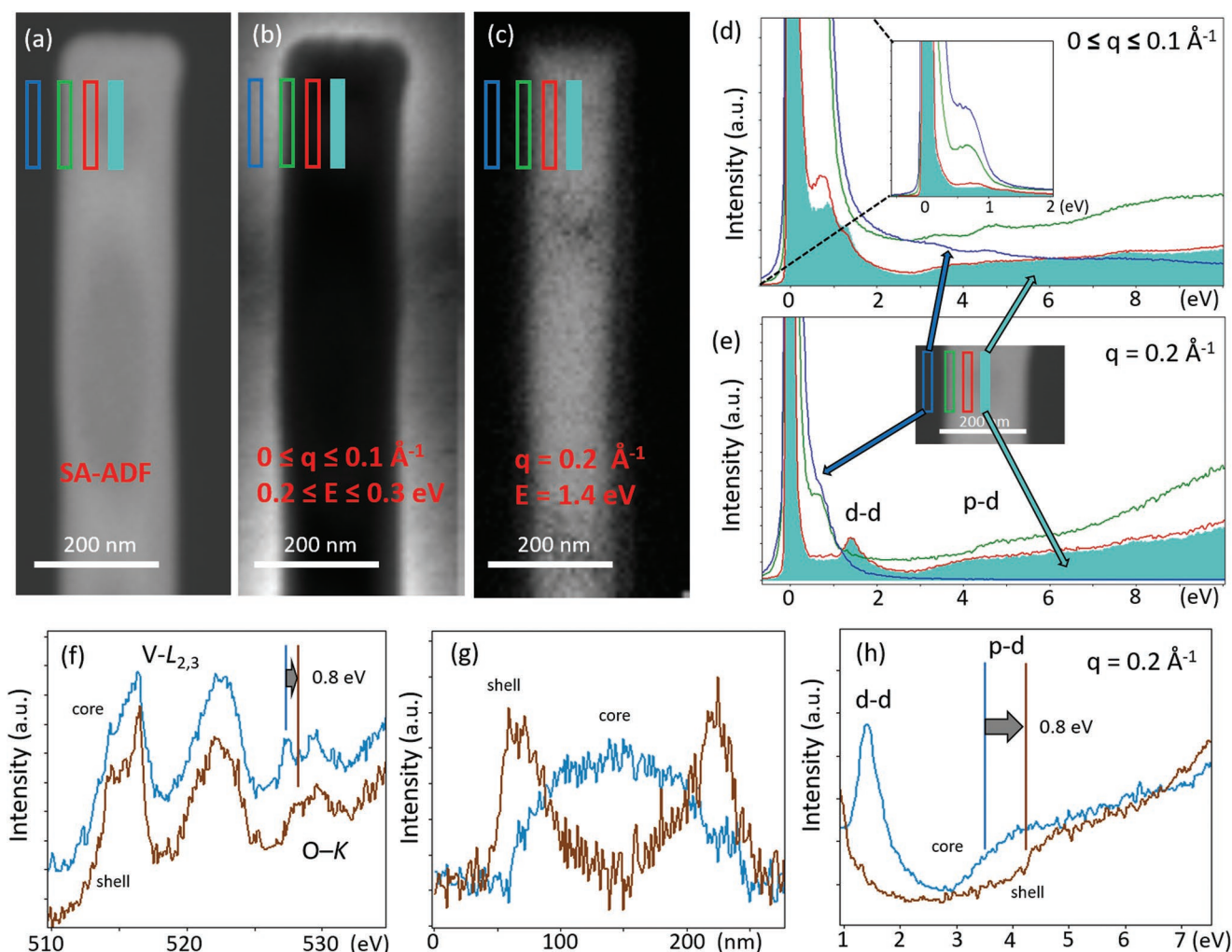
Figure 5. a) Small-angle annular dark field (SA-ADF) image of the tip of a ≈ 2.6 µm long half-rod. b) EELS energy map obtained in dipolar condition at low-energy showing surface plasmon modes. c) EELS energy map obtained in non-dipolar condition at the energy of 1.4 eV corresponding to the bulk-type d–d plasmon. d,e) Spectra extracted at different positions as indicated in the images for the dipolar and non-dipolar conditions. The inset in (d) shows the presence of an intense surface plasmon measured at the shell or in the vacuum in dipolar condition. f) V-L and O-K EELS edges measured at the core and shell position, g) the corresponding profiles of the fitting weights of the core and shell EELS components in (f). h) EELS spectra measured at the core and shell position in non-dipolar condition. The d–d plasmon is suppressed in the shell while the p–d excitation is blueshifted.

The final point concerns the potential of EELS to measure the bulk plasmonic properties of transition oxides at a nanometer scale. It is of interest for the mapping of MIT in, for example, VO_2 or a nickelate ($ANiO_3$ with A being a rare earth element), but also possibly to determine the local TM 3d band occupation and doping evolution by measuring plasmonic shifts. As discussed in the first part of the article, SVO exhibits a weak bulk plasmon dispersion and the surface plasmon intensity is reduced to a negligible contribution by off-dipolar conditions.

Figure 5a–c exhibits a dark-field STEM image and two corresponding energy maps obtained for dipolar (0.2 eV $\leq E \leq$ 0.3 eV and $q \leq 0.1$ Å^{-1}) and non-dipolar ($E = 1.4$ eV and $q = 0.2$ Å^{-1}) EELS condition measured at the tip of a long half-rod (≈ 2.6 µm). The dark-field image exhibits diffraction contrast since it corresponds to the small-angle annular dark-field image (collection angles of ≈ 4 to 8 mrad) due to the projectors lenses setting required for the q-resolved experiment. The dipolar EELS map

(0.2 eV $\leq E \leq$ 0.3 eV) evidences surface plasmon modes similarly as discussed in the previous part (e.g., Figure 3a). The non-dipolar EELS map obtained at 1.4 eV evidences the presence of the bulk plasmon in the central part of the rod section. Figure 5d,e compares the dipolar and non-dipolar spectra at different lateral positions near the tip of the rod as shown in the maps. Wherever the position of the EELS spectra, almost no bulk plasmon contribution is visible for dipolar condition (Figure 5d) while intense surface plasmons are detected everywhere including in aloof position (dark blue square). On the other hand, a strong bulk-type excitation is measured in the central part (plain cyan curve) and up to ≈ 30 nm from the surface for non-dipolar EELS (Figure 5e). Near the surface, the bulk d–d plasmon excitation disappears and only a faint surface plasmon is present (green curve of Figure 5e) that is further vanishing in the vacuum. Figure 5f,g shows the V-$L_{2,3}$ and O-K EELS excitations typical of the core and shell areas of the rods

with their corresponding spatial distribution across a profile. The core can be considered as a representative of the bulk SVO electronic structure while a thick shell of ≈30 nm displays a different electronic structure. In that shell, the V-L edges display more resolved multiplet lines and the splitting of the O-K pre-peak is reduced while its edge onset is blueshifted at ≈0.8 eV. The shell corresponds to the amorphized area (as determined by electron diffraction) due to the FIB beam damage. The reduction of the O-K pre-peak splitting that is partially a finger-print of the crystal field strength in TMOs is in agreement with this structural aspect since amorphous oxides are expected to have a weaker crystal field than a dense phase such as perov-skite. The shift of the onset of the O-K edge and the narrowing of the multiplet lines might also evidence a bandgap opening at the shell. Disordered (e.g., cation or oxygen-depleted SVO)[47] or ultra-thin SrVO₃ films[5] are indeed known to experience MIT. Figure 5h compares the low energy excitations obtained at the non-dipolar condition for areas corresponding to the core and the shell. As stated before, the bulk d–d plasmon has totally disappeared in the shell (while not being replaced by a surface plasmon contribution) and the p–d charge transfer type excitation exhibits a shift of 0.8 eV in perfect agreement with the O-K shift. It is additional evidence that the disordered shell has a different electronic structure from bulk SVO, probably associated with an MIT. Furthermore, the spatial distribution of the low-energy excitations of Figure 5h is identical to the core-loss spatial distribution (Figure S5, Supporting Information) confirming that non-dipole EELS can efficiently probe the bulk-type electronic structure in SVO. It is envisioned that similar EELS measurement of the bulk low-energy excitations can be feasible for most of the TMO nanostructures whose small bands and plasmons dispersions are similarly expected.

3. Conclusion

Our STEM–EELS experiments demonstrate that the narrow and strong 1.35 eV peak in the SrVO₃ loss function is a bulk plasmon with small energy dispersion. The ab initio calculation reveals that a 1.5 band renormalization is enough to reproduce quantitatively the plasmon energy within a TDDFT theoretical framework. LSPs have been observed for many several nano-structures (slab, slit, half-rod) and the measured quality factors indicate that SVO is a promising material for IR plasmonic technology, exceeding most of the doped oxide semiconduc-tors. The presence of plasmon hot spots is visible by EELS at the protuberances and it might result in field enhancement on granular thin films or for chemically obtained SrVO₃ parti-cles, for example, via sol–gel route.[48] Finally, mixed spatial and angular resolved EELS can be done to phase out the strong sur-face plasmon retrieving bulk properties. It has revealed a core–shell structure associated with metal–insulator distributions in SVO nanostructures designed by FIB.

4. Experimental Section

Sample Preparation: The sample was a SrVO₃ single crystal grown with the floating zone technique. Microparticles were obtained by crushing small pieces of the single crystal. Slabs and nanostructures were obtained by Ga-FIB polishing from the single crystal. Slabs were obtained in a similar approach as conventional TEM lamella preparation but preparing them with different controlled thicknesses. The final polishing of the slab was done with a 2 keV Ga beam to reduce the damaged surface layers. Nanostructures (half-rods, slits) were then obtained by FIB nano-machining of the slabs with a Ga beam of 30 keV.

STEM–EELS: STEM–EELS measurements were done using a monochromated Nion microscope operated at 100 keV. EELS data were collected using a CMOS detector optically coupled to a scintillator (Figures 1–4) or a direct electron detector (MerlinEM from QuantumDetectors, Figure 5). Thicknesses were estimated using the so-called "t-over-lambda" technique and a mean free path was estimated according to Malis et al.[49] The EELS with high spatial resolution were typically done with convergence semi-angles of 25 or 10 mrad (e.g., Figures 2 and 3) and corresponding collection semi-angles of ≈40 and 20 mrad. Dispersion curves were obtained by reducing the convergence semi-angle below 1 mrad and the collected angles were varied by displacing the diffraction pattern in front of the EELS entrance aperture (e.g., Figure 1b,c) but similar results were obtained using a slit in the diffraction plane. Mixed angular and spatially resolved EELS were obtained with convergence semi-angles between 1.5 (e.g., Figure 5) and 3 mrad. An energy resolution of typical 40 meV was used and no deconvolutions were done to reduce this instrumental broadening. In Figure 1a, the black spectrum, corresponding to a very thick area and a larger energy window, was deconvoluted from the plural scattering contribution.

Ab Initio: TDDFT calculations adopted the same computational framework already validated by Ruotsalainen et al.[36] Additionally, the d–d plasmon dispersion in Figure 2d was obtained with a finer 20 × 20 × 20 grid of k points.

FTTD: The EELS spectra were then simulated using the FDTD method as described in Cao et al.[25] and more details on the procedure can be found in Figures S6 and S7, Supporting Information. The dielectric function ε of SVO for the FDTD calculations was obtained from the ab initio calculations. For comparison of all the −ε′/ε″ of Figure 4, the other dielectric functions were obtained from Werner et al.[50] and Naik et al.[51]

Supporting Information

Supporting Information is available from the Wiley Online Library or from the author.

Conflict of Interest

The authors declare no conflict of interest.

Data Availability Statement

The data that support the findings of this study are available from the corresponding author upon reasonable request.

[1] L. Zhang, Y. Zhou, L. Guo, W. Zhao, A. Barnes, H.-T. Zhang, C. Eaton, Y. Zheng, M. Brahlek, H. F. Haneef, N. J. Podraza, M. H. W. Chan, V. Gopalan, K. M. Rabe, R. Engel-Herbert, *Nat. Mater.* **2016**, *15*, 204.

[2] Y. Park, J. Roth, D. Oka, Y. Hirose, T. Hasegawa, A. Paul, A. Pogrebnyakov, V. Gopalan, T. Birol, R. Engel-Herbert, *Commun. Phys.* **2020**, *3*, 102.

[3] A. Boileau, A. Cheikh, A. Fouchet, A. David, R. Escobar-Galindo, C. Labbé, P. Marie, F. Gourbilleau, U. Lüders, *Appl. Phys. Lett.* **2018**, *112*, 021905.

[4] B. Bérini, V. Demange, M. Bouttemy, E. Popova, N. Keller, Y. Dumont, A. Fouchet, *Adv. Mater. Interfaces* **2016**, *3*, 1600274.

[5] A. Fouchet, M. Allain, B. Bérini, E. Popova, P.-E. Janolin, N. Guiblin, E. Chikoidze, J. Scola, D. Hrabovsky, Y. Dumont, N. Keller, *Mater. Sci. Eng., B* **2016**, *212*, 7.

[6] H. Makino, I. H. Inoue, M. J. Rozenberg, I. Hase, Y. Aiura, S. Onari, *Phys. Rev. B* **1998**, *58*, 4384.

[7] M. Mirjolet, H. B. Vasili, L. López-Conesa, S. Estradé, F. Peiró, J. Santiso, F. Sánchez, P. Machado, P. Gargiani, M. Valvidares, J. Fontcuberta, *Adv. Funct. Mater.* **2019**, *29*, 1904238.

[8] A. Boileau, A. Cheikh, A. Fouchet, A. David, C. Labbé, P. Marie, F. Gourbilleau, U. Lüders, *Adv. Opt. Mater.* **2019**, *7*, 1801516.

[9] S. Choi, J. Kang, S. Ryu, H. Jeen, J. Son, S. Lee, *APL Mater.* **2020**, *8*, 041111.

[10] K. Maiti, U. Manju, S. Ray, P. Mahadevan, I. H. Inoue, C. Carbone, D. D. Sarma, *Phys. Rev. B* **2006**, *73*, 052508.

[11] S. Aizaki, T. Yoshida, K. Yoshimatsu, M. Takizawa, M. Minohara, S. Ideta, A. Fujimori, K. Gupta, P. Mahadevan, K. Horiba, H. Kumigashira, M. Oshima, *Phys. Rev. Lett.* **2012**, *109*, 056401.

[12] K. Morikawa, T. Mizokawa, K. Kobayashi, A. Fujimori, H. Eisaki, S. Uchida, F. Iga, Y. Nishihara, *Phys. Rev. B* **1995**, *52*, 13711.

[13] M. J. Rozenberg, I. H. Inoue, H. Makino, F. Iga, Y. Nishihara, *Phys. Rev. Lett.* **1996**, *76*, 4781.

[14] E. Pavarini, S. Biermann, A. Poteryaev, A. I. Lichtenstein, A. Georges, O. K. Andersen, *Phys. Rev. Lett.* **2004**, *92*, 176403.

[15] M. Karolak, T. O. Wehling, F. Lechermann, A. I. Lichtenstein, *J. Phys.: Condens. Matter* **2011**, *23*, 085601.

[16] M. Gatti, M. Guzzo, *Phys. Rev. B* **2013**, *87*, 155147.

[17] L. Boehnke, F. Nilsson, F. Aryasetiawan, P. Werner, *Phys. Rev. B* **2016**, *94*, 201106.

[18] K. Nakamura, Y. Nohara, Y. Yosimoto, Y. Nomura, *Phys. Rev. B* **2016**, *93*, 085124.

[19] J. Kim, Y. Zhao, G. V. Naik, N. K. Emani, U. Guler, A. V. Kildishev, A. Alu, A. Boltasseva, in *CLEO: 2013-OSA Technical Digest (online)*, Optica Publishing Group, Washington DC, USA **2013**.

[20] M. Bauch, T. Dimopoulos, S. Trassl, *Nanotechnology* **2019**, *30*, 265201.

[21] M. Bosman, E. Ye, S. F. Tan, C. A. Nijhuis, J. K. W. Yang, R. Marty, A. Mlayah, A. Arbouet, C. Girard, M.-Y. Han, *Sci. Rep.* **2013**, *3*, 1312.

[22] V. Mkhitaryan, K. March, E. N. Tseng, X. Li, L. Scarabelli, L. M. Liz-Marzán, S.-Y. Chen, L. H. G. Tizei, O. Stéphan, J.-M. Song, M. Kociak, F. J. García De Abajo, A. Gloter, *Nano Lett.* **2021**, *21*, 2444.

[23] D. Preziosi, L. Lopez-Mir, X. Li, T. Cornelissen, J. H. Lee, F. Trier, K. Bouzehouane, S. Valencia, A. Gloter, A. Barthélémy, M. Bibes, *Nano Lett.* **2018**, *18*, 2226.

[24] C. Ullrich, *Time-Dependent Density-Functional Theory: Concepts and Applications*, OUP Oxford, Oxford, UK **2012**.

[25] Y. Cao, A. Manjavacas, N. Large, P. Nordlander, *ACS Photonics* **2015**, *2*, 369.

[26] M. Zhang, N. Large, A. L. Koh, Y. Cao, A. Manjavacas, R. Sinclair, P. Nordlander, S. X. Wang, *ACS Nano* **2015**, *9*, 9331.

[27] Y. K. Sato, M. Terauchi, K. Adachi, *J. Appl. Phys.* **2019**, *126*, 185107.

[28] H. Raether, *Excitation of Plasmons and Interband Transitions by Electrons*, Springer, New York **1980**.

[29] J. Gong, R. Dai, Z. Wang, Z. Zhang, *Sci. Rep.* **2015**, *5*, 9279.

[30] K. J. Krane, *J. Phys. F: Met. Phys.* **1978**, *8*, 2133.

[31] S. Suto, K.-D. Tsuei, E. W. Plummer, E. Burstein, *Phys. Rev. Lett.* **1989**, *63*, 2590.

[32] G. Nicotra, E. Van Veen, I. Deretzis, L. Wang, J. Hu, Z. Mao, V. Fabio, C. Spinella, G. Chiarello, A. Rudenko, S. Yuan, A. Politano, *Nanoscale* **2018**, *10*, 21918.

[33] A. vom Felde, J. Sprösser-Prou, J. Fink, *Phys. Rev. B* **1989**, *40*, 10181.

[34] P. Cudazzo, M. Gatti, A. Rubio, *Phys. Rev. B* **2012**, *86*, 075121.

[35] D. E. McNally, X. Lu, J. Pelliciari, S. Beck, M. Dantz, M. Naamneh, T. Shang, M. Medarde, C. W. Schneider, V. N. Strocov, E. V. Pomjakushina, C. Ederer, M. Radovic, T. Schmitt, *npj Quantum Mater.* **2019**, *4*, 6.

[36] K. Ruotsalainen, M. Gatti, J. M. Ablett, F. Yakhou-Harris, J.-P. Rueff, A. David, W. Prellier, A. Nicolaou, *Phys. Rev. B* **2021**, *103*, 235158.

[37] B. C. Larson, W. Ku, J. Z. Tischler, C.-C. Lee, O. D. Restrepo, A. G. Eguiluz, P. Zschack, K. D. Finkelstein, *Phys. Rev. Lett.* **2007**, *99*, 026401.

[38] M. Cazzaniga, H.-C. Weissker, S. Huotari, T. Pylkkänen, P. Salvestrini, G. Monaco, G. Onida, L. Reining, *Phys. Rev. B* **2011**, *84*, 075109.

[39] R. Sakuma, P. Werner, F. Aryasetiawan, *Phys. Rev. B* **2013**, *88*, 235110.

[40] M. Takizawa, M. Minohara, H. Kumigashira, D. Toyota, M. Oshima, H. Wadati, T. Yoshida, A. Fujimori, M. Lippmaa, M. Kawasaki, H. Koinuma, G. Sordi, M. Rozenberg, *Phys. Rev. B* **2009**, *80*, 235104.

[41] F.-P. Schmidt, H. Ditlbacher, U. Hohenester, A. Hohenau, F. Hofer, J. R. Krenn, *Nat. Commun.* **2014**, *5*, 3604.

[42] B. Ögüt, R. Vogelgesang, W. Sigle, N. Talebi, C. T. Koch, P. A. Van Aken, *ACS Nano* **2011**, *5*, 6701.

[43] V. Kapetanovic, I. C. Bicket, S. Lazar, M. J. Lagos, G. A. Botton, *Adv. Opt. Mater.* **2020**, *8*, 2001024.

[44] E. L. Runnerstrom, A. Bergerud, A. Agrawal, R. W. Johns, C. J. Dahlman, A. Singh, S. M. Selbach, D. J. Milliron, *Nano Lett.* **2016**, *16*, 3390.

[45] H. Yang, A. Konečná, X. Xu, S. W. Cheong, E. Garfunkel, F. J. García de Abajo, P. E. Batson, *Small* **2022**, *18*, 2106897.

[46] P. R. West, S. Ishii, G. V. Naik, N. K. Emani, V. M. Shalaev, A. Boltasseva, *Laser Photonics Rev.* **2010**, *4*, 795.

[47] G. Wang, Z. Wang, M. Meng, M. Saghayezhian, L. Chen, C. Chen, H. Guo, Y. Zhu, E. W. Plummer, J. Zhang, *Phys. Rev. B* **2019**, *100*, 155114.

[48] P. Lei, J. Liu, S. Zhuge, Z. Lü, *Mater. Lett.* **2022**, *333*, 133575.

[49] T. Malis, S. C. Cheng, R. F. Egerton, *J. Electron. Microsc. Tech.* **1988**, *8*, 193.

[50] W. S. M. Werner, K. Glantschnig, C. Ambrosch-Draxl, *J. Phys. Chem. Ref. Data* **2009**, *38*, 1013.

[51] G. V. Naik, V. M. Shalaev, A. Boltasseva, *Adv. Mater.* **2013**, *25*, 3264.